Journal of Nuclear Materials 381 (2008) 211–215

Contents lists available at ScienceDirect

Journal of Nuclear Materials

journal homepage: www.elsevier.com/locate/jnucmat

Nanoscale characterization of HT-9 exposed to lead bismuth eutectic at 550 °C for 3000 h

P. Hosemann [a,b,*], M.E. Hawley [b], D. Koury [c], J. Welch [c], A.L. Johnson [c], G. Mori [a], N. Li [b], S.A. Maloy [b]

[a] CD Laboratory of Localized Corrosion, University of Leoben, Franz-Josef Strasse 18, 8700 Leoben, Austria
[b] Los Alamos National Laboratory, P.O. Box 1663, Los Alamos, 87544 NM, USA
[c] University of Nevada Las Vegas, 4505 S. Maryland Parkway, Las Vegas, NV 89154, USA

ARTICLE INFO

Article history:
Received 22 October 2007
Accepted 28 March 2008

ABSTRACT

Fast reactors and targets in spallation neutron sources may use lead bismuth eutectic (LBE) as a coolant. Its physical and chemical properties and irradiation properties make it a safe and high performance coolant in radiation environments. However, LBE is a corrosive medium for most steels. In the present study, the atomic force microscopy, magnetic force microscopy, conductive atomic force microscopy, surface potential microscopy, and scanning electron analysis with energy dispersive X-ray spectroscopy were performed to get a better understanding of the corrosion and oxidation mechanism of the HT-9 stainless steel in an LBE environment. What was believed in the past to be simply a double oxide layer structure was revealed here to be more complicated. It is found that the inner most oxide layer maintains the grain structure of what used to be the bulk steel material while the outer oxide layer possessed a columnar structure. The EDS line scans and the conductive and magnetic properties measured using the scanning probe techniques give us the local properties of the formed oxide layers. This leads to a more detailed view of the oxide layers formed on HT-9 in LBE.

1. Introduction

Lead bismuth eutectic (LBE) has a low melting point, low chemical reactivity, low vapor pressure, low viscosity, good gamma shielding, and high spallation neutron yield, make LBE an ideal candidate coolant for fast reactors and spallation sources. The main requirement for using LBE as a coolant is the understanding and controlling of the corrosion of candidate steels and container materials in contact with LBE. In an oxygen controlled LBE environment a protective oxide layer can be formed on a variety of different steels [1–3] in order to substantially reduce further corrosion. This protective layer needs to be able to withstand this environment for a long period of time (40+ years for reactors) to ensure safe and reliable operation. To guarantee this, it is important to understand the growth mechanism of the oxide layers with detailed analyses. In this study micro- and nanoscale analytical techniques are used to investigate the structure and properties of the oxide layer formed on the HT-9 steel (HT-9) in an LBE environment at 550 °C in order to get a better understanding of how this layer is formed and the reliability of these oxide layer to protect the underlying steel.

2. Experiment

2.1. LBE loop exposure

An HT-9 steel tube was exposed to flowing LBE in the test loop at the Institute of Physics and Power Engineering (IPPE) in Obninsk, Russia. The composition of this material is 11.95% Cr, 1% Mo, 0.6% Mn, 0.57% Ni, 0.5% W, 0.4% Si, 0.33% V, and 0.2% C by weight with the balance in Fe. It was suggested by [4] and demonstrated by [5,6] that ferritic/martensitic (F/M) steels like HT-9 are radiation tolerant. The HT-9 tube was tested at 550 °C in 2 m/sec flowing LBE containing 10^{-6} wt% oxygen for 3000 h. The IPPE loop has a very stable operation history and few fluctuations in operation (changes in temperature or flow) were reported. The oxygen content in the LBE was monitored using yttria stabilized zirconia membrane sensors with bismuth oxide reference electrodes while the oxygen replenishment was done using a solid phase oxygen control system [7]. The LBE flow direction was parallel to the tube length. After exposure, the tubes were cut into 5 mm long pieces and embedded in epoxy. The samples were polished using a 0.1 μm colloidal silica as the last step on a Buehler Vibromet2 polisher. The root-mean-square (RMS) surface roughness measured on 3 × 3 μm areas by the atomic force microscopy (AFM) on sample cross section sample at the outer layers was 1–1.2 nm. This provided a flat and smooth surface necessary for scanning probe characterization. The samples were analyzed in cross section using the AFM, magnetic force microscopy (MFM), conductive atomic

* Corresponding author. Address: Los Alamos National Laboratory, P.O. Box 1663, Los Alamos, 87544 NM, USA. Tel.: +1 505 629 9893; fax: +1 505 667 7443.
E-mail address: peterh@lanl.gov (P. Hosemann).

0022-3115/$ - see front matter © 2008 Elsevier B.V. All rights reserved.
doi:10.1016/j.jnucmat.2008.03.018

force microscopy (C-AFM), scanning electron microscopy (SEM) and energy dispersive X-ray (EDX) spectroscopy, and wavelength dispersive X-ray spectroscopy (WDS).

2.2. AFM and MFM measurements

The AFM and MFM measurements on the various oxide layers were performed at the Los Alamos National Laboratory (LANL) using a Veeco Metrology Nanoscope IIIa controller and D3000 microscope. The tips used for these measurements were commercial silicon Tapping Mode™ cantilevers with CoCr magnetic coated tips. The imaging scan rate was generally $\leqslant$0.4 Hz for a 40 μm × 40 μm surface area (i.e. lower resolution images) and adjusted to a higher raster frequency for smaller scan size images. The resonance frequencies of these tips were around 65 kHz. The topographic and corresponding magnetic images were taken simultaneously at the exact same location. The MFM characterization was used to distinguish various oxide layers by differences in their magnetic properties.

2.3. Potential and C-AFM measurements

The AFM, potential and C-AFM measurements were also performed at LANL using a Veeco Metrology Nanoscope IV controller and a D3100 microscope equipped with a C-AFM application module. C-AFM is a contact mode electrical characterization technique that involves applying a voltage, typically, between the conductive AFM tip and the sample while monitoring variations in the local electrical properties in a range of pA to μA. Surface potential characterization was also performed on the Nanoscope IV. All measurements were performed on the same sample in approximately the same area used for the MFM measurements using the same type of cantilevers in order to correlate structural, magnetic, and electrical properties with each other and with the chemical composition data.

2.4. SEM/EDS measurements

The SEM/EDX and WDS measurements were performed at the University of Nevada, Las Vegas (UNLV) using a JEOL 5610 scanning electron microscope (SEM/EDX) and a JEOL JXA-8900R Electron Probe Microanalyzer for the WDS analysis. Elemental maps and line scans were performed using EDS and WDS. In most cases the EDX data were sufficient. In instances where spectral overlap was a concern, WDS was used to confirm the EDS measurement (e.g. in a typical EDX energy spectrum, Mn K_α and K_β peaks overlap the K_β of Cr and K_α of Fe, respectively). The acceleration voltage in both the SEM and the Electron Probe was 15 kV, and both types of measurements were taken at a working distance of 20 mm.

3. Results

Surface probe characterization revealed the presence of 4 distinct oxide layers, which were formed on the surface of the HT-9 stainless steel after exposure to the LBE eutectic. The AFM, MFM and C-AFM results on the oxide layers are presented in Figs. 1–5. It can be clearly seen from these images that a multi-layer structure is present, similar to that reported in the literature [1,2]. These

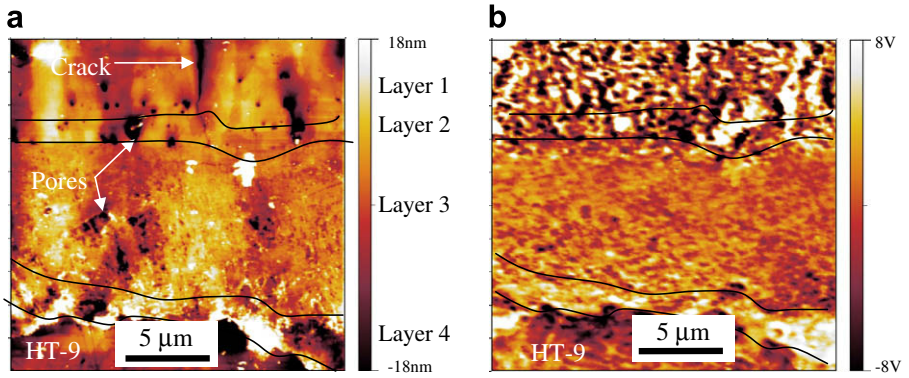

Fig. 1. AFM topography image (a) and corresponding MFM image (b) of HT-9 after 3000 h in LBE.

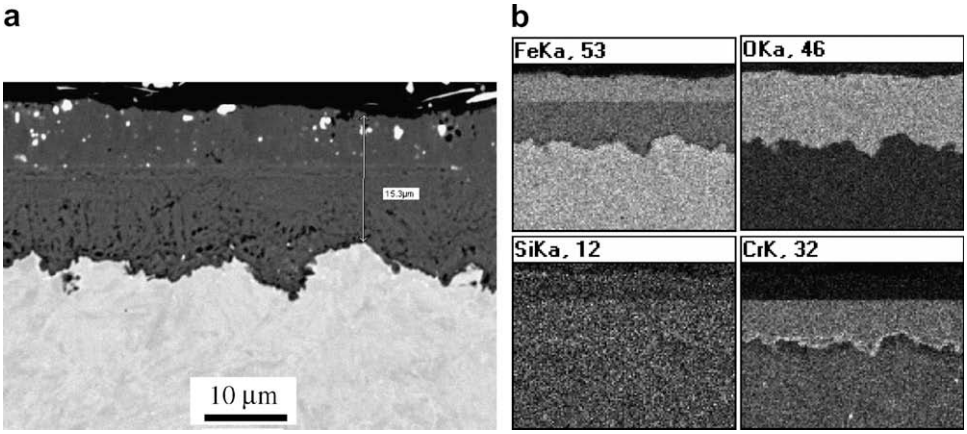

Fig. 2. Back scattered SEM image (a) and EDX mapping (b) of the same location on HT-9 exposed to 550 °C LBE for 3000 h.

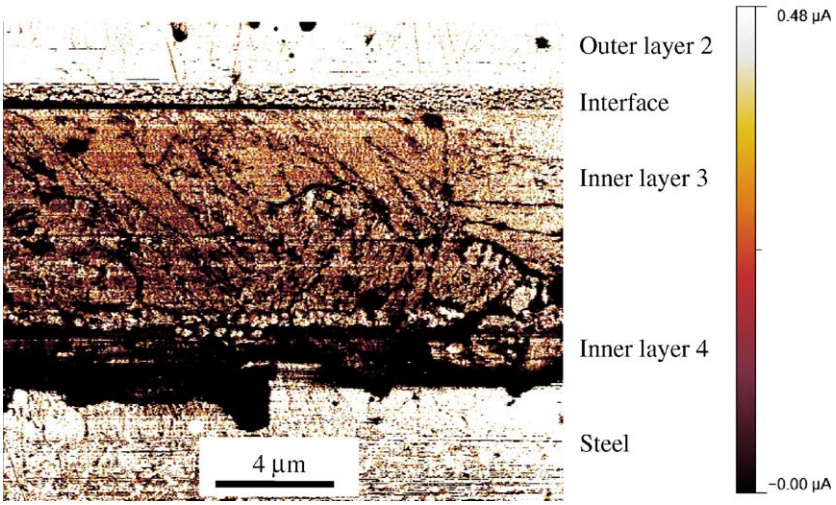

Fig. 3. C-AFM image of all oxide layers. The color scale is shown to the right. Bright colors represent high current while dark colors show low current. (For interpretation of the references to colour in this figure legend, the reader is referred to the web version of this article.)

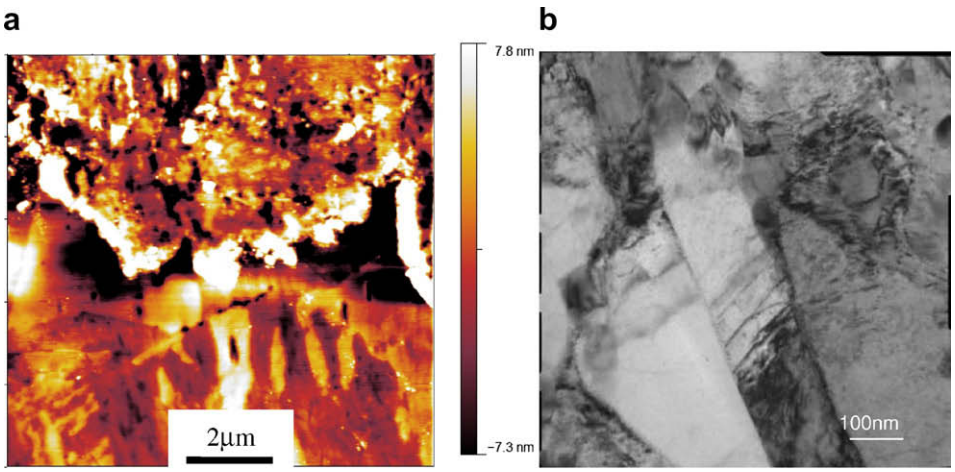

Fig. 4. AFM image of the steel and the inner oxide layer (a) and TEM image of the martensitic structure in HT-9 (b).

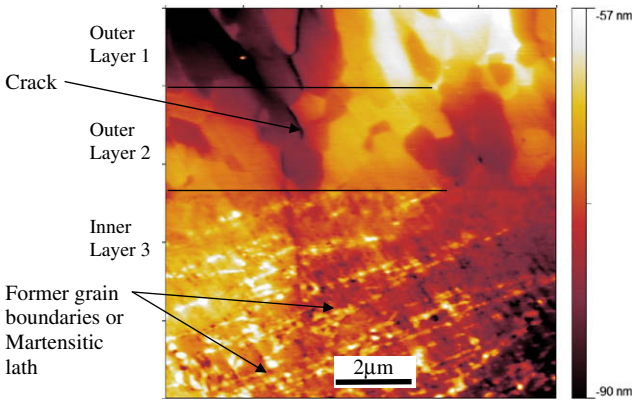

Fig. 5. AFM image of the oxide layers grown in LBE.

detailed AFM, MFM and C-AFM structural and corresponding property images allow one to distinguish between these 4 different types of oxide layers. The outer layer can be divided in two distinct areas based on a change in grain structure (outer layer 1 and outer layer 2) (see Fig. 5). The AFM topography reveal that the grains in outer layer 1 (400–700 nm wide and 1–5 μm long) are elongated and oriented approximately perpendicular to the sample surface while the grains in outer layer 2 are more round in shape (500 nm–1.5 μm in size). Large deep pores were detected within both outer layer 1 and outer layer 2. The pores were mostly found at grain boundaries but pores within grains were also observed. The thickness of outer layer 2 is between 2 and 4 μm while the total outer layer thickness is between 6 and 10 μm. In several areas cracks were observed extending from the surface towards the inner layer. These cracks appear to be at the grain boundaries. There was no or little evidence that the cracks or pores were filled with LBE.

The C-AFM allows us to measure qualitatively the local conductivity. In the C-AFM image presented bright colors refer to a high current passing through the sample (refers to higher conductivity) while dark colors show low current passing through the sample (low conductivity). The corresponding scale is shown by the image. These measurements revealed that the outer layer 2 is conductive (Fig. 3). The grain boundaries can still be seen in the C-AFM image as less conductive. The SEM/EDX measurements show that no Cr is present in the outer layers. The amount of Fe and O found leads to the assumption that the outer layers are probably pure Fe_3O_4 (magnetite) The MFM images show that these outer layers have

a strong magnetic domain structure, which is also consistent with them being magnetite.

The inner layer 3 shows clearly a different microstructure from the outer layers. The cross sectional surface analysis of the inner layer also appears much rougher than the outer layers. The entire inner layer has a relatively high pore density. It seems there is also a pore size gradient within the inner layer. Towards the outer surface, the pores are smaller (mean pore size is 84 nm) and very finely dispersed (pore density is 5.4 pores/μm^2). Towards the bulk steel side the pores become larger (mean pore size is 123 nm), the pore density becomes smaller (pore density is 4.5 pores/μm^2). High structures (20–50 nm) were found within the inner oxide layer. It appears that these structures are lined up and correlate with the grain boundaries and martensitic lath interfaces in the steel. The grain boundaries in this layer are not visible in the MFM image.

The C-AFM image (Fig. 3) shows that the inner layer is not as conductive as the outer layer. The taller aligned structures (possible previous steel grain boundaries or martensitic lath interfaces) are visible as non conductive lines in the inner layer. The SEM/EDX clearly shows Cr enrichment in this layer and at the grain boundaries where the non conductive lines were found.

The interface between inner layer and bulk steel (layer 4) shows a strong Cr enrichment using the SEM/EDX, while the C-AFM also indicates that it is non conductive. The topographic images of this area reveal that there are higher structures at the transition from the inner oxide layer to steel. This boundary, although well-defined, is not straight but rather meandering possibly following the original grain boundaries.

The steel itself has a surface RMS roughness of about 2–3 nm. This means an excellent surface preparation is needed for this kind of measurements. No cracks were observed in the inner layer close to the bulk steel or in the steel itself. Fig. 4 compares the measured martensitic lath interface using AFM with martensitic laths measured on the same materials using TEM [8]. It is shown that the structure and size between TEM and AFM image are comparable. At the grain boundaries or marthensitic lath interfaces in the bulk steel close to the oxide layer small pores were detected.

4. Discussion

The AFM/MFM and C-AFM images clearly show that the outer oxide layer does not correspond to the grain structure of the steel in any way and, therefore, is newly grown. The fact that the SEM/EDX measurements show only Fe and O in the outer layer and that this outer layer is conductive and strongly magnetic leads to the assumption that the outer layer is Fe_3O_4 because Fe_3O_4 is electrically conductive (e.g. $\sim 10\ \Omega^{-1}\ cm^{-1}$ at $\sim 90\ ^\circ C$) above the transition temperature (119 K) [9,10]. It is found that the outer layer grain structure changes from a globular grain to an elongated grain closer to the surface. So far it is not clear what causes this change in grain structure but it is assumed that as the outer oxide layer grows thicker, the Fe has to diffuse further to reach the surface and, therefore, less Fe arrives at the surface. This can lead to a slower oxide layer growth which might lead to more oriented grains in the diffusion direction. Cracks going through the outer layer always followed the grain boundaries, which show that the failure mechanism of the layer is due to intergranular cracking.

The oxide layer 3 can be divided in two regions as well. Close to the layer 3 and layer 2 interface is a region (<1 μm thick) with a different and very fine structure of electrical property difference (see Fig. 3). This was only found on a few scan locations. It is not entirely clear what causes this interface. But since the interface between layer 3 and layer 2 is the original steel interface and was in contact with the LBE at an earlier stage as it was described elsewhere [13], this change might be caused by the direct contact between Fe–Cr spinel and LBE. Because the inner layer 3 reflects the grain structure of the steel it is assumed here that the inner layer 3 adopts the steel grains by O diffusion inwards. Very low electrical conductivity lines and precipitate-like particles can be seen at the grain boundaries. It is known that higher Cr content in any kind of spinel or as addition to Fe_3O_4 reduces the conductivity [10]. This and the fact that Cr enrichment was found in these areas as well suggests that Cr_2O_3 precipitates or another Cr rich phase (like $FeCr_2O_4$) at these boundaries are responsible for the low conductivity. It is found in [9] that the difference in electrical conductivity between Fe_3O_4 and $FeCr_2O_4$ is 4 orders of magnitudes. Therefore the C-AFM can be used to map out small variations in composition on a large area.

It was observed that some of the cracks, starting in the outer oxide layer, reach deep into the inner oxide layer as well. The area of layer 3 closer to the layer 3 and layer 4 interfaces preferentially contains a large number of pores at the grain boundaries or martensitic laths interfaces. This explains the soft behavior in nanoindentation tests from previous studies [11,12].

The oxide layer 4 (between layer 3 and steel) is insulating as it can be seen in Figs. 3 and 6. The SEM/EDS also shows high Cr enrichment (Fig. 2). This suggests that Cr segregates to this interface and forms a ~1–2 μm wide area between oxide layer and steel

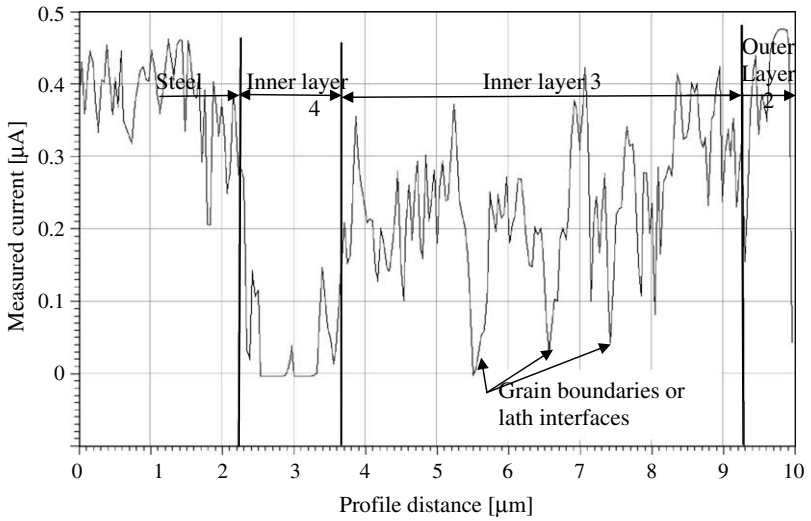

Fig. 6. Line profile of the C-AFM measurements.

which is Cr_2O_3 or Cr rich spinels like $FeCr_2O_4$. The steel itself is shown to be highly conductive as expected. A line profile from all the oxide layers (starting from the steel going into the outer oxide layer 2) shows that the grain boundary itself and the steel–inner oxide interface layer are highly insulating compared to the grains themselves. At this point no quantitative statement regarding the conductivity of the oxide layers can be made using C-AFM.

Considering the results obtained from AFM/MFM/C-AFM and SEM/EDX the following statements are proposed.

The inner oxide layers (3 and 4) adopt the grain structure from the bulk steel. High pore density within these layers suggests that these are fast diffusion paths allowing Fe diffusing outwards and O diffusing inwards. The Cr rich areas at the grain boundaries suggest that either the Fe was removed (diffusion outwards) or Cr was enriched. The outer oxide layer forms a new grain structure which is consistent with a newly formed oxide layer. The pores found in the bulk steel and the Cr rich area in between the bulk steel and the oxide layer suggest that Cr segregates from the steel to the oxide layer. It is not likely that the excess of Cr originates from the oxide layer since no increase in electrical conductivity was found. It appears that the oxide layers grown in the LBE environment follow a similar mechanism as proposed in [13]. Only the fact that the Cr content is lower in HT-9 than in the D9 steel studied there and that HT-9 has more interfaces due to its martensitic structure can account for the different appearance and growth rate of the oxide layers formed.

5. Conclusions

- AFM, MFM and C-AFM were successfully used to characterize the oxide layers formed on HT-9 steel in LBE.
- It was found that the oxide consists of at least 4 different layers with different grain structure or conductivity/magnetic properties.
- The outer layers seem to be Fe_3O_4 and have good conductivity while the inner layer is Cr enriched and has lower conductivity or insulating. This is in agreement with the literature where Cr additions lower the conductivity of Fe_3O_4.
- It was found that the steel grain boundaries and martensitic lath interfaces are still visible in the inner oxide layers. These boundaries are highly insulating. The interface between steel and inner oxide layer is highly insulating as well.
- It is proposed that the oxide layer growth mechanism is similar to what is described in [13] for D9 stainless steel.

References

[1] J. Zhang, N. Li, Y. Chen, A.E. Rusanov, J. Nucl. Mater. 336 (2005) 1.
[2] H. Glasbrenner, J. Konys, G. Mueller, A. Rusanov, J. Nucl. Mater. 296 (2001) 1.
[3] P. Hosemann, H.T. Thau, A.L. Johnson, S.A. Maloy, N. Li, J. Nucl. Mater. 373 (2008) 246.
[4] K. Herschbach, W. Schneider, C. Wassilew, Atomenergie/Kerntechnik 36 (1980) 4.
[5] F.A. Garner, M.B. Toloczko, B.H. Sencer, J. Nucl. Mater. 276 (2000) 123.
[6] Stuart A. Maloy, M.B. Toloczko, K.J. McClellan, T. Romero, Y. Kohno, F.A. Garner, R.J. Kurtz, A. Kimura, J. Nucl. Mater. 356 (2006) 62.
[7] Handbook on Lead–bismuth Eutectic Alloy and Lead Properties, Materials Compatibility, Thermal-hydraulics and Technologies, OECD/NEA 2007 Edition.
[8] C. Vieh, P. Hosemann, R.R. Greco, S.A. Maloy, LANL Internal Report, 2008.
[9] B. Gillot, F. Jemmali, A. Rousset, J. Mater. Sci. 21 (1986) 4436.
[10] J.H. Park, K. Natesan, Oxid. Met. 33 (1990) 31.
[11] P. Hosemann, S.A. Maloy, N. Li, Fortschr. Metall. 38 (2006).
[12] P. Hosemann, J.G. Swadener, J. Welch, N. Li, J. Nucl. Mater. 376 (3) (2008) 289.
[13] P. Hosemann, M. Hawley, D. Koury, J.G. Swadener, J. Welch, A.L. Johnson, G. Mori, N. Li, J. Nucl. Mater., doi: 10.1016/j.jnucmat.2007.12.005.